# Nanoscale

Accepted Manuscript


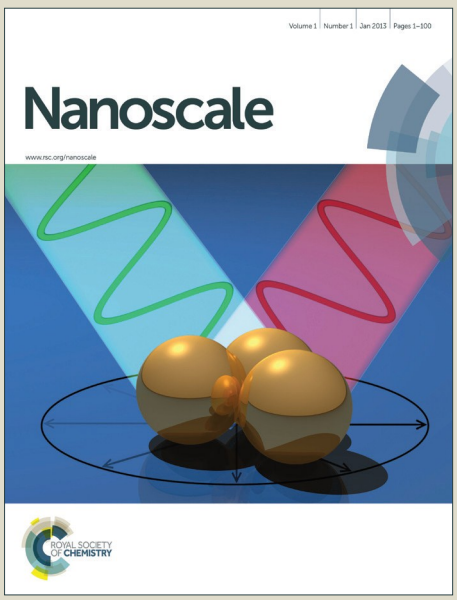





ROYAL SOCIETY OF CHEMISTRY

www.rsc.org/nanoscale

Cite this: DOI: 10.1039/c0xx00000x

www.rsc.org/xxxxxx

ARTICLE TYPE

# Facile and Generalized Encapsulations of Inorganic Nanocrystals with Nitrogen-doped Carbonaceous Coating for Multifunctionality

**Yong Yang, Jingchao Zhang, Shitong Wang, Xiaobin Xu, Zhicheng Zhang, Pengpeng Wang, Zilong Tang, Xun Wang ***

***Received (in XXX, XXX) Xth XXXXXXXXX 20XX, Accepted Xth XXXXXXXXX 20XX***
**DOI: 10.1039/b000000x**

A simple strategy toward versatile encapsulations of inorganic nanocrystals, through a green hydrothermal treatment of commercial polyurethane sponge, was developed. This approach enables us to realize a general method to form surface-adherent, N-doped coating with a controllable thickness for well-defined structures. These composites exhibit active properties in optical application and energy storage. For example, N-doped carbon encapsulated $Fe_2O_3$ nanoboxes show very high discharge capacity and outstanding cyclability, and the capacity still remained 1,086 mA h $g^{-1}$ at a current density of 400 mA $g^{-1}$ after 200 cycles. Our results described here provide a simple surface coating technique so as to design various functional nanostructures.

## Introduction

Nitrogen doped carbon nanomaterials (N-CMs) with controlled morphologies show great advantages in many applications, including catalyst supports,[1] bioimaging,[2] $CO_2$ sequestration,[3] supercapacitors[4] and oxygen reduction reaction,[5-8] owing to the increase of the surface polarity, electrical conductivity and electron-donor tendency.[9-10] Particularly, first-principle calculations have revealed that interfacial stability and electric conductivity of inorganic nanocrystals can be significantly enhanced through N-doped carbon coating.[11] So far, various coating methods have been reported to design the surface properties in order to enhance their stability and improve their conductivity.[12] Up to now, effective control of N-doped carbon coating has proven challenging. In this regard, a facile and general method to encapsulate inorganic nanocrystals with N-doped carbon coating is highly desirable. In this work, we present a simple yet general hydrothermal carbonization process of polyurethane (PU) sponge to encapsulate inorganic nanocrystals with N-doped carbonaceous coating for the first time.

PU sponge, the most commonly used shock absorption materials, is widely used since the 1930s. PU sponge is composed of a chain of organic units joined by carbamate links. Due to their special three-dimensional (3-D) porous structures, PU sponge has been used as a template to synthesize hybrid composites.[13-18] Nevertheless, this hardly-decomposed compound usually leads to serious resource wastes and environmental pollution due to inappropriate disposal techniques.[19] Taking green chemistry and sustainable development into consideration, it is of extreme urgency to develop a low-cost and environment-friendly method to make use of PU sponge.

In this report, we present a simple strategy toward versatile encapsulations of inorganic nanocrystals with nitrogen-doped carbonaceous coatings, through a green hydrothermal treatment of commercial PU sponge. The highly porous 3-D structures of PU sponge may serve as ideal platforms for homogenous absorption of other species like inorganic nanocrystals, and as a result this hydrothermal process leads to forming surface-adherent coating with a controllable thickness. In addition, nitrogen can be in situ introduced into the carbonaceous coating layer because of the rich N of the PU sponge. This N-doped carbonaceous coating layer can act as a unique medium for optical application and an excellent conductor in energy storage after carbonization. As a proof of concept, we demonstrate that the surface plasma properties of Au nanoparticles can be finely tuned by changing the thickness of coatings. Moreover, the Au/N-C composites were used as a surface-enhanced Raman scattering (SERS) substrate and showed enhanced SERS effect as compared to the pure Au nanoparticles. Most importantly, the N-doped carbon encapsulated $Fe_2O_3$ nanoboxes exhibit very high discharge capacity and outstanding cycling performance as an anode material for lithium ion battery (LIBs). It is believed that the present study not only provides a versatile method to control surface coating for inorganic nanocrystals, but also allows for the design of functional composites for a broad range of applications.

## Results and Discussion

PU sponge used in this work was first cleaned and cut into small cubes (Fig. S1). N-doped carbonaceous coating hybrid composites can be obtained by introducing various nanocrystals before hydrothermal treatment (Fig. 1a). The coating structure

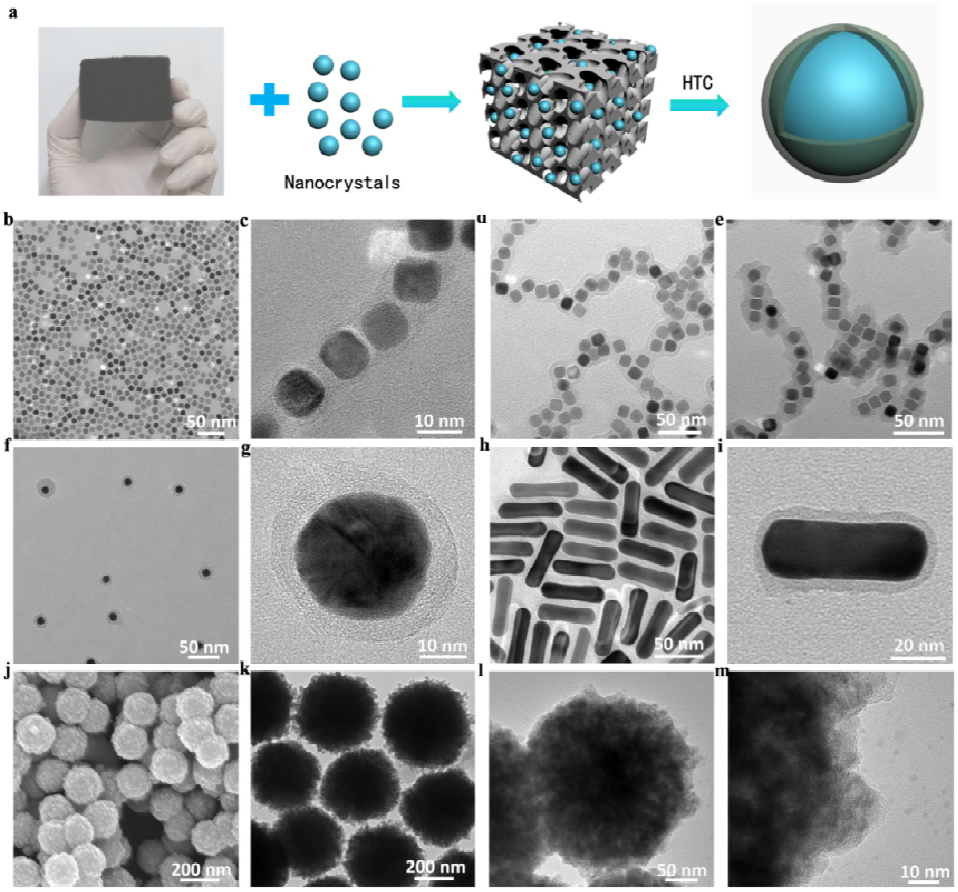


**Fig1**. (a) Schematic illustration of the formation of nanocrystals with N-doped carbonaceous coating. (b) TEM imags of Pd nanocubes. TEM images of the different thickness of Pd coated N-doped carbon obtained after 1 h (c), 2 h (d) and 3 h (e) of hydrothermal treatment. (f-g) TEM images of AuNPs coated N-doped carbon layer under different magnifications. (h-i)TEM images of pristine Au nanorods and Au nanorods coated N-doped carbon. (j-m) SEM and TEM images of CdS with N-doped carbonaceous coating.

was initially investigated with 8 nm Pd nanocube (Fig. 1b). As shown in Fig. 1c, Pd nanocube has been encapsulated by a very thin shell structure, displaying chain-like topology. The thickness of coating layer is around 1 nm. It was noted that the coating thickness was tunable by varying the reaction time. The coating thickness was a function of the hydrothermal time and reached 10 nm after 3 hours (Fig. 1c-e). Most importantly, we found that the encapsulation strategy can be extended to various nanostructured species with different sizes, and shapes (Fig. S2), including Au nanoparticles (AuNPs), Pt nanocaves, $MnO_2$ nanowires, carbon nanotubes (CNTs), $Fe_2O_3$ nanoboxes (120 nm), $Fe_2O_3$ nanoplates (150 nm) and CdS nanoparticles (250 nm). These nanocrystals were successfully coated by a N-doped carbonaceous layer using this approach without any surface modification (Fig. S3). All composites exhibited well-defined structure with excellent water dispersibility. Fig. 1g presents the TEM images of AuNPs coated by a shell thickness of about 5 nm. We noted that the small-sized nanoparticles tend to form chain-like nanoassemblies after coating, especially in the coating of nanoparticles less than 10 nm. In this case, we can see that these small-sized Pd nanocubes tend to embed into a chain geometry structure. Conversely, there was a core-shell structure for large-sized nanoparticles. For example, CdS and $Fe_2O_3$ nanoboxes can be individually encapsulated by a carbonaceous layer (Fig. 1i-k). Even for the one-dimensional structure, the CNTs and $MnO_2$ nanowires can be covered by a layer with cable-like structure (Fig. S3e-f). This implies that the encapsulation of N-doped carbonaceous coating has no relationship with the morphology of nanocrystals.

X-ray photoelectron spectroscopy (XPS) was used to investigate the structural information of coating layer. The survey spectrum of the Pd/N-C shows three typical peaks of $C_{1s}$, $N_{1s}$, and $O_{1s}$ (Fig. S4). The corresponding $C_{1s}$ spectrum in Fig. 2a shows four peaks at 284.6, 285.7, 286.6, and 288.0 eV,[20] which is assigned to C–C, C–N, C–O, and C=N/C=O, respectively. The high-resolution N1s spectrum (Fig. 2b) indicates the presence of C-N-C (398.5 eV) and N-C3 (399.6 eV), [21] indicating that the nitrogen atom has been well doped into the carbon skeleton. The Pd/N-C was further characterized by Raman spectroscopy (Fig. S4d), the two broad bands located at 1351 and 1577 $cm^{-1}$ represented the D band and G band, respectively. The low $I_D/I_G$ ratio, $I_D/I_G \approx 1.0$, indicates the presence of graphic phase and shows that the graphitic level is not very high after hydrothermal treatment. As disclosed by the FTIR spectrum in Fig. S5, the broad peak centered at 3400 $cm^{-1}$ was assigned to O–H or N–H vibrations. Bands at around 1370 and 1504 $cm^{-1}$ for all the N-doped-encapsulated composites correspond to the C-NH-C/C=C stretching modes, which are consistent with the XPS results.

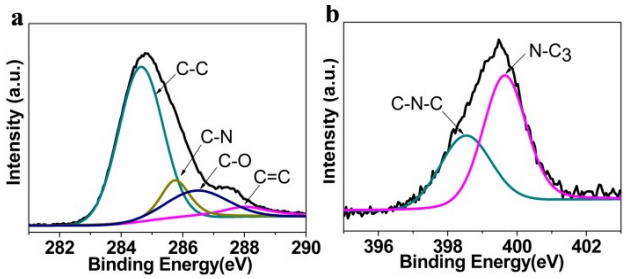


**Fig 2**. (a) High-resolution C1s of XPS spectra of the as-prepared Pd/N-C. (b) High-resolution N1s of XPS spectra of the as-prepared Pd/N-C.

decomposing of PU sponge during hydrothermal treatment. As shown in Fig. S6a, the pristine PU sponges possess three-dimensional and well-connected networks. After hydrothermal treatment, a lot of hemispheric structures emerge on the surface of PU skeleton at 200 $^{o}$C for 2 h (Fig. S6b-c). A yellow solution was formed during this stage, which shows that PU decomposed into some monomers. After reacting for 6 h (Fig. S6d), some micro-sized sheet structures can be seen and the 3-D structure of PU sponge was completely changed, indicating ongoing polymerization or condensation reactions. As the reaction proceeds (Fig. S6e-f), it was obvious to see that only irregular structure can be obtained after 12 h, which results from the polymerization and carbonization of PU sponge. XPS measurements were used to determine the composition of the product after hydrothermal treatment. Compared with pristine PU sponge, we found that the content of the oxygen of the fianal product is still very high (26.82%), indicating the low dehydrogenation and condensation degree during this process (Table S1). It is speculated that PU sponge degrade into monomers through a top-down process during the hydrothermal treatment. When nanocrystals were added into the solution, these polymeric fragments may absorb on the surface of species, giving rise to a surface-adherent layer. This is similar to the hydrothermal carbonization of carbohydrates and other biomass materials.[22-23] We therefore speculate that this is generalized hydrolysis and polymerization of PU sponge under hydrothermal treatment. Firstly, PU sponge will degrade into monomers through a top-down process under subcritical conditions. Then, these monomers or polymeric fragments may assemble or absorb on the surface of the nanocrystals and other species in solution via a cross-linking or π-π packing reaction,[24-29] leading to surface-adherent, N-doped coating layer. In order to illustrate the versatility of the strategy, we used different PU sponge as carbon sources to encapsulate CNTs. The result showed that all CNTs can be successfully coated by a carbonaceous layer under the same conditions (Fig. S7).

**Photoelectric property of nanocomposites**

We first applied this coating technique for noble metal to investigate their optical properties. We coated the AuNPs with N-doped carbonaceous coating because AuNPs are one of the most extensively investigated metals due to their unique localized surface plasmon resonances (SPR).[30-31] In a typical experiment, citrate-stabilized 8-nm-diameter AuNPs were prepared and redispersed in water to desired concentrations. The TEM images are presented in Fig. 3a. The AuNPs have been encapsulated within cross-linked layer after coating. It is noted that the small-sized nanoparticles tend to form chain-like nanoassemblies after coating (inset in Fig. 3a), which is consistent with the Pd/N-C composites. To further study the shift of the plasmon resonant wavelength as a function of coating thickness, time-dependent experiments were investigated by TEM analysis and UV-vis absorption measurements. It is obvious to see that the thickness of the coating layer increased with time (Fig. S8) and the color of AuNPs solution gradually changed from reddish to bluish violet over time (Fig. 3b). The corresponding UV-vis spectra shows a gradual red-shift (Fig. 3c), which is in good agreement with the theoretical prediction that SPR is usually influenced by the refractive index of the surrounding medium, and its strength decreases as the refractive index increases.[32-33] Similar plasmon shifts can be observed for different diameter of AuNPs after coating (Fig. S9a-f). In addition, the thinkness of coating layer can also be changed by varying the amount of PU spnge ((Fig. S9e-g). As a result, surface plasmon resonances of AuNPs can be continuously tuned by changing the thickness of coating layers. Cyclic voltammogram results (Fig. S10) indicate that the existence of Au structure at about 0.9 V gives rise to some electrochemical response. On the other hand, there was no peak about 0.9 V, indicating AuNPs/N-C composites possess pinholes-free character.

Encouraged by this pinholes-free character, we demonstrated the application of 55-nm-diameter Au/N-C composites as a substrate for SERS. As shown in Fig. 3d, a high-contrast Au core was covered with a layer of ca. 2 nm thickness, displaying a well-defined core-shell structure. This coating layer can be further proved by EDS line scanning profiles across an individual particle(Fig. S10e-f). The SERS performance of Au/N-C composites is five times higher than that of pure AuNPs (Fig. 3e). Enhanced SERS performance may be associated with their enhanced ability to absorb more aromatic dye molecules.[34] This ultrathin shell not only can provide a physical barrier to against the aggregation of AuNPs, but also enhance interaction with the probe molecules via π-π stacking interaction because of abundant functional groups on the coating surface (Fig. 3f). However, a thick layer undoubtedly reduces the Raman signal. When the shell thickness increases to ca. 10 nm, the signal intensity decrease remarkably due to the near-field effect of localized SPR (Fig. S11c).[35]

This coating can also be used as a protective layer for CdS. CdS was an excellent candidate as anode materials in the photo electrochemical cells. However, CdS usually suffers from poor stability because the sulfide ion is highly prone to oxidation. We coated CdS nanoparticles with a thin layer (CdS/N-C) as a protection layer to prevent the oxidation of sulfide ions. TEM image revealed that CdS were uniformly coated by a thin layer (Fig. 3g). Diffuse reflectance spectroscopy was used to characterize the absorption property of the CdS nanoparticles after coating. CdS/N-C show enhanced visible-light absorption compared with the pure CdS nanoparticles (Fig. 3h). We studied their photocurrent-density response under visible-light and the photocurrent measure showed that the performance of CdS/N-C was about three times than that of pure CdS nanoparticles (Fig. 3i). In order to investigate the effect of the coating, we examined the crystallographic structure of CdS/N-C composites before and after heat treatment in air. After being coated, the obtained materials were further annealed at 450°C in air. The calcinated

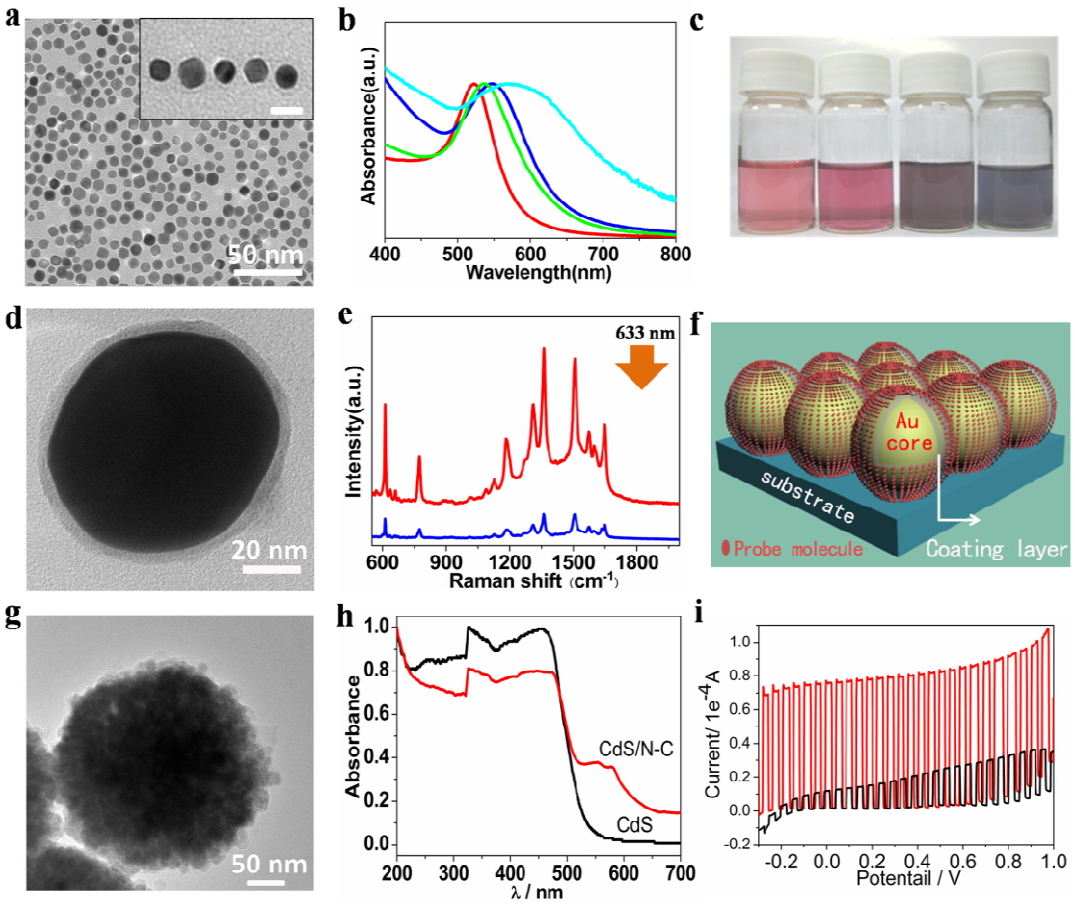


**Fig 3.** (a) TEM image of 8-nm-diameter AuNPs. The inset is Au/N-C composite after surface coating, displaying a chain geometry structure. Scale bars: 10nm. (b) UV-vis extinction spectra of Au/N-C composite under different time from left to right, 0 min, 40 min, 80 min, and 120 min. (c) The corresponding color of Au/N-C. (d) HRTEM image of 55-nm-diameter AuNPs/N-C. (e) SERS spectra of Au/N-C of ca. 2 nm shell (red) and pure AuNPs (blue) at 633 nm laser excitation. (f) AuNPs/N-C adsorbed by probed molecules: contact mode. (g) TEM image of CdS with N-doped carbonaceous coating. (h) Diffuse reflectance UV/Vis spectra of pure CdS and CdS/N-C hybrid composites. (i) Photocurrent-density response. I-V scans of under visible-light illumination of pure CdS nanoparticles (black) and as-synthesized CdS/N-C composite heated in air (red).

hybrid materials still exhibited diffraction patterns identical to that of pure CdS (Fig. S12), indicating that CdS is not oxidized at high temperatures. This is similar to previous work about carbon-coated CdS nanostructures.[36] Therefore, enhanced photocurrent performance can be attributed to the N-doped carbonaceous coating, which serves as a resistant against oxidation so as to preserve the inner CdS nanoparticles through surface engineering method.

### Lithium ion battery test of $Fe_2O_3$/N-C nanoboxes nanocomposites

We further explored the application of $Fe_2O_3$ nanoboxes with N-doped carbon coating ($Fe_2O_3$/N-C) in lithium ion battery. $Fe_2O_3$ nanoboxes were first prepared by annealing prussian blue nanocubes (Fig. 4a).[37] After coating, a uniform layer can be clearly seen around the entire surface of $Fe_2O_3$ nanoboxes. The structure and composition of $Fe_2O_3$ nanoboxes can be well retained based on the observation of TEM images (Fig.S14) and XPS spectra (Fig. 4b-d). The survey spectrum of the $Fe_2O_3$/N-C shows four typical peaks of $C_{1s}$, $N_{1s}$, $O_{1s}$ and $Fe_{2p}$ (Fig. 4e). The XPS spectrum shows that the content of the nitrogen of $Fe_2O_3$/N- C is as high as 10.18 wt%. In addition, the $Fe_{2p}$ peaks of $Fe_2O_3$ nanocubes at ~711 eV and ~725 eV are contributed to Fe 2p3/2 and Fe 2p1/2 for iron(III) oxide (Fig. 4f). The as-obtained sample was further treatmented followed by thermal annealing in $N_2$. The synthetic procedure for $Fe_2O_3$/N-C is presented in Fig. S13 and the carbon content is calculated to be about 15 wt% by thermogravimetric analysis (Fig.S15).

Fig. 5a depicts the cycling behavior of the $Fe_2O_3$/N-C and $Fe_2O_3$ nanoboxes electrodes. It is worth noting that the $Fe_2O_3$/N-C the electrode can still deliver a capacity of 1,225 mA h $g^{-1}$ at a current density of 200 mA $g^{-1}$ after 150 cycles. By contrast, the capacities of the pure $Fe_2O_3$ nanoboxes was about 717 mA h $g^{-1}$. The capacities of $Fe_2O_3$/N-C are much higher than $Fe_2O_3$ nanoboxes, indicating that this N-doped carbon coating can effectively improve the Li-cycling kinetics, thus leading to a higher capacities. Note that the capacity of $Fe_2O_3$/N-C and $Fe_2O_3$ displays an increasing trend. The increasing trend of the capacity of material is likely associated with a gradual activation process of the metal-oxide electrodes as well as the reversible growth of the polymeric gel-like film by the kinetically activated electrolyte

degradation, which is a common phenomenon for metal-oxide anode materials.[38-42] Fig. 5b shows the rate capability of the as-obtained $Fe_2O_3$/N-C at different current densities. It can be clearly observed that the as-obtained composits display excellent capacity retention at different rates.

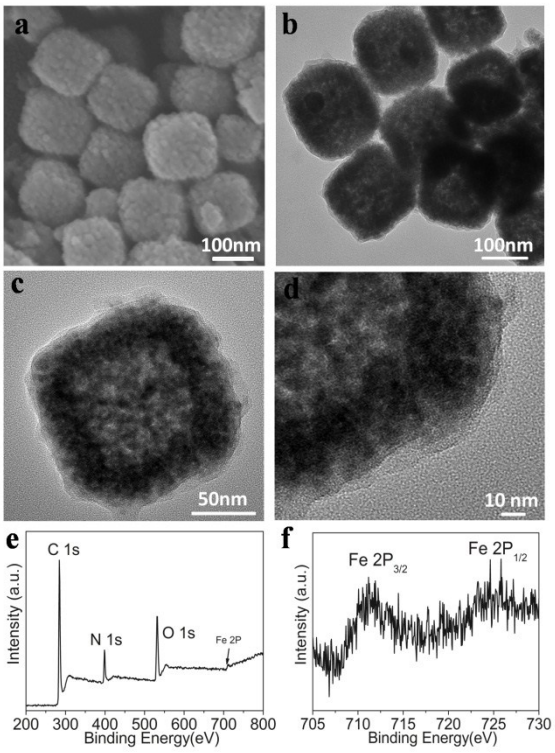


**Fig 4.** (a) SEM images of the as-prepared $Fe_2O_3$ nanoboxes. (b-d) TEM images of the $Fe_2O_3$/N-C nanoboxes under different magnifications. e) XPS spectra of $Fe_2O_3$/N-C nanoboxes. f) XPS Fe 2p spectrum of $Fe_2O_3$/N-C nanoboxes.

The voltage profiles of $Fe_2O_3$/N-C nanoboxes at a current density of 400 mA $g^{-1}$ are shown in Fig. 5c. The discharge−charge voltage profiles are typical characteristics of the voltage feature for the $Fe_2O_3$ electrode, which is attributed to the reversible reduction of $Fe^{3+}$ to $Fe^0$ and the formation of $Li_2O$ based on the following reaction: $Fe_2O_3+6Li^++6e^- \rightleftarrows 2Fe^0+3Li_2O$. [43-45] The initial capacity loss may be attributed to the incomplete conversion reaction and irreversible lithium loss. Moreover, the $Fe_2O_3$/N-C electrode is still able to deliver a capacity of 1086 mAh $g^{-1}$ after 200 cycles at a density of 400 mA $g^{-1}$ (Fig. 5d). It is clear that the capability of $Fe_2O_3$/N-C hybrid is superior to those iron oxide-based anodes results previously reported, such as carbon-coated CNT@$Fe_2O_3$,[46] 3D $Fe_3O_4$/graphene foams,[40] $Fe_2O_3$/3D graphene networks,[47] and $Fe_2O_3$@polyaniline.[48]

We also investigated the cycling response at varying rates, as shown in Fig. S16. Even during cycling at a high current density of 1000 mA $g^{-1}$ after 150 cycles, their capacities could still be retained over 720 mA h $g^{-1}$, which exhibits an outstanding energy storage performance (high capacity and long cycle life) as an anode material for LIBs. This remarkable improvement of the cycling performance can be associate with the size of $Fe_2O_3$ nanoboxes and the N-doped carbon coating.[45] We believe that the N-doped coating layer here not only serves as mechanical reinforcement so as to dissipate the stress caused by the volume excursions in charging and discharging reactions, but also increases the electrical conductivity because of the high content of nitrogen. As a consequence, $Fe_2O_3$/N-C delivers a high reversible capacity and remarkable cycling performance. In short, this N-doped carbon coating technique shows wide promising applications in energy storage and conversion.

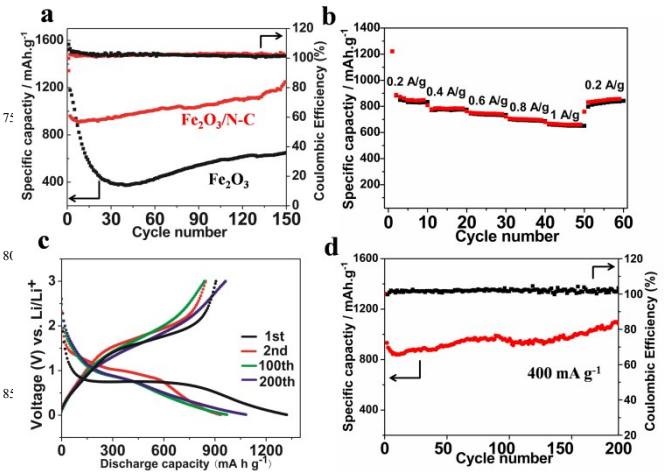


**Fig 5.** (a) Discharge-charge voltage profiles of $Fe_2O_3$/N-C. (b) Rate capability of $Fe_2O_3$/N-C at various current densities. (c) Discharge-charge voltage profiles of $Fe_2O_3$/N-C at a current density of 400 mA $g^{-1}$. (d) Long-term cycling stability of $Fe_2O_3$/N-C. Tests are conducted between 0.01 and 3.0 V.

## Conclusion

In summary, we have demonstrated an effective and green strategy to control N-doped carbonaceous coating through hydrothermal approach of commercial PU sponge in water for the first time. This encapsulation strategy technique is applicable to various nanocrystals with a controllable thickness. We note that precursors used in the process are abundant and available, which meet the commercial needs for scale-up production. The resulting composites exhibit a variety of properties, and their potential applications in optical property and energy storage have been investigated. As an example, we demonstrate that the surface plasma properties of AuNPs can be finely tuned by changing the thickness of coating layer. The resulting nanocomposits also exhibit enhanced SERS performance compared with pure Au nanoparticles. What is more, the N-doped carbon coating can significantly increase the performance of lithium ion battery. Therefore, this encapsulation strategy described in this work has great advantages in designing functional composites for various applications including biosensors, catalysis and energy storage and conversion applications.

## Experimental section

**Synthesis of 8 nm AuNPs**[49]: Typically, PVP (K30, 50 mg) and $H_2C_2O_4$ (0.5 mmol, 63 mg) were successfully dissolved into formamide (5 mL) and heated to 120 °C. Then $HAuCl_4 \cdot 4H_2O$ aqueous solution (0.25 mL, 0.2 mol/L) was quickly injected into the above solution, the solution turned dark red immediately and was maintained at 120 °C for 10 min. After cooling, the product was washed with acetone and centrifuged two times. The final product could be well dispersed in water.

**Synthesis of 13 nm AuNPs**[50]**:** Citrate-stabilized AuNPs were prepared by a sodium citrate reduction method of $HAuCl_4$. In a typical procedure for the synthesis of 13 nm AuNPs, an aqueous solution of $HAuCl_4$ (0.01%, 150 ml) was brought to a vigorous boil with rapid stirring in a round bottom flask (250 ml). When the solution started to boil, an aqueous solution of trisodium citrate (1%, 4.5 ml) was added. The deep red suspension can be obtained under stirring for another 30 minutes. Other AuNPs with different diameters were prepared by changing the amounts of trisodium citrate (1%, 4.5 ml) while other conditions are kept constant. For example, 55-diameter AuNPs were prepared by changing an aqueous solution of trisodium citrate (1%, 1 ml). The deep red suspension can be obtained under stirring for 30 minutes.

**Synthesis of Au nanorods:** Gold nanorods were synthesized using a two-step seed-mediated method described previously. [51] Briefly, 10 mL of an aqueous 0.25 mM solution of $HAuCl_4 \cdot 3H_2O$ was added into 7.5 mL of an aqueous 0.1 M cetyltrimethylammonium bromide solution. Then, 0.6 mL of an aqueous 0.01 M ice-cold $NaBH_4$ solution was added and stirred for 2 min. The seed solution was kept in a water bath at 25 °C and was used at least 2 h. Second, 12 μL of seed solution was added to solution containing 0.1 M CTAB, 0.5 mM $HAuCl_4$, 0.55 mM ascorbic acid, and 0.06 mM silver nitrate. The reaction mixture was mixed and left undisturbed for 12h. The solution of NRs was centrifuged to remove the excess CTAB and redispersed in deionized water.

**Synthesis of Pd nanocubes**[49]**:** KI (166 mg) and PVP (K30, 50 mg) were added into 5 mL of formamide under intense stirring at 120°C. Then, $PdCl_2$ powder (65 mg) was added and maintained at 120°C for 60 min. After the reaction, 20 mL acetone was added and the dispersion was centrifuged at 10000 rpm for 5min. The washing was repeated for several times. The final product could be well dispersed in water.

**Synthesis of Pt concaves**[52]**:** 2 mL of $H_2PtCl_6$ solution (20 mM), PVP (K30, 200 mg), and glycine (40 mg) were added to 6.0 mL of deionized water and stirred several minute at room temperature. The resulting yellow homogeneous solution was transferred to a 12 mL Teflon-lined stainless-steel autoclave and heated at 200°C for 6h. After cooling, the product was washed with water several times to remove all soluble impurities. The final product could be well dispersed in water.

**Synthesis of α-$MnO_2$ nanowires**[53]**:** Manganese sulphate monohydrate ($MnSO_4 \cdot H_2O$), ammonium persulfate ($(NH_4)_2S_2O_8$), and ammonium sulfate $(NH_4)_2SO_4$ with a molar ratio of 1:1:3 was added into 36 ml of distilled water under intense stirring and transferred to a Teflon vessel held in a stainless steel vessel. The sealed vessel was placed in an oven and heated at 180°C for 12h. After cooling, the product was washed with water several times to remove all soluble impurities, and finally dried in air at 80 °C.

**Synthesis of $Fe_2O_3$ nanoboxes:** $Fe_2O_3$ nanoboxes were obtained by the annealing of prussian blue nanocubes.[36] Firstly, $K_4Fe(CN)_6 \cdot 3H_2O$ (45mg), polyvineypirrolydone (PVP, K30, MW ~ 30000, 3.0 g) and were added to a HCl solution (0.1 M, 30 mL) under magnetic stirring. A clear solution was obtained by stirring for 30 min. The bottle was then placed into an electric oven and heated at 80 °C for 15 h. The obtained blue product was washed with distilled water and absolute ethanol for several times and finally dried in air at 60 °C for 12 h. To convert the prussian blue nanocubes into hollow $Fe_2O_3$ microboxes structures, the as-synthesized prussian blue product was heated at different temperature of 550 °C with a temperate ramp of 1 °C $min^{-1}$ for 10 h in air.

**Synthesis of $Fe_2O_3$ nanoplates**[54]**:** $FeCl_3 \cdot 6H_2O$ (1.0 mmol) was dissolved under vigorously magnetic stirring in ethanol (10.0 mL) and distilled water (0.7 mL). Then, 0.8 g of sodium acetate was added under stirring. The mixture was sealed and transferred to a Teflon vessel held in a stainless steel vessel. The sealed vessel was placed in an oven and heated at 180°C for 12h. After cooling, the red solid products were washed with distilled water and ethanol several times, and finally dried in air at 60 °C.

**Synthesis of CdS nanoparticles**[35]**:** $CdCl_2 \cdot 6H_2O$ (3.5 mmol), thiourea (3.5 mmol), and polyvinylpyrrolidone (PVP; MW~ 58K, 0.5 g) were dissolved in 30 mL of ethylene glycol (EG) under intense stirring. This homogeneous mixture was then transferred into a Teflon-lined stainless-steel autoclave of 50 mL in capacity and kept at 160 °C for 12h in an electric oven. After cooling, the yellow products were collected by centrifugation, washed with ethanol and distilled water, and finally dried in air at 80 °C.

**Synthesis of nanocrystals with nitrogen-doped carbonaceous coating:** Firstly, the commercial PU sponge was obtained after being washed with water and ethanol, and then dried in air. Typically, a certain amount of nanoparticles, including Pd, Au, Pt, $MnO_2$ nanowires, CNTs, $Fe_2O_3$ nanoboxes, $Fe_2O_3$ nanoplates and CdS nanoparticles, were dissolved in 30 mL of water. Then, the prepared PU sponge was added. The solution was transferred to a 50 mL Teflon-lined stainless steel autoclave and sealed. The autoclave was then heated at 180-200°C for several hours. After cooling, the product was collected by removing the insoluble materials through simple filtration. Finally, the product was harvested by centrifugation, washed with water. The products were named as Pd/N-C, Au/N-C, Pt/N-C, $MnO_2$/N-C, CNTs/N-C CdS /N-C and $Fe_2O_3$/N-C.

**Materials Characterization:** The morphology and size of the nanostructures were determined by a HITACHI H-7700 TEM with an accelerating voltage of 100 kV, and a FEI Tecnai G2 F20 S-Twin high-resolution (HR) TEM equipped with energy dispersive spectrometer (EDS) analyses at 200 KV. The samples were prepared by depositing and evaporating a droplet of the aqueous colloidal solution on silicon pellet or a carbon-coated copper grid. The scanning electron microscope (SEM) was performed on a LEO 1530. The crystal structure was analyzed by a Bruker D8-advance X-ray powder diffractometer operated at 40 kV voltage and 40 mA current with CuKα radiation (λ=1.5406 Å). IR spectra were measured by using a Perkin Elmer FT-IR spectrophotometer on KBr pellets in the range of 4000-400 $cm^{-1}$ with the resolution of 4 $cm^{-1}$. The C, H and N contents were measured on a VarioEL (ElementarAnalysensysteme GmbH). X-ray photoelectron spectroscopy (XPS) experiments were carried out on scanning X-ray microprobe (Quantera SXM, ULVAC-PHI. INC) operated at 250 kV, 55 eV with monochromated Al Kα radiation. The diffuse reflectance ultravioletvisible (UV-vis) absorption spectrum were obtained using a Shimadzu UV-3600 spectrometer. Thermo-gravimetric analysis was carried out at a constant heating rate of 10 °C $min^{-1}$ from room temperature to 800 °C on a TA-50 thermal device in air. Raman spectrometer employing an Ar-ion laser operating at 514 nm. A 50×, telephoto

Olympus objective lens, was used to focus the laser on the samples (laser spot size: ca. 2 μm). All spectra were calibrated with respect to silicon wafer at 520.7 $cm^{-1}$.

**SERS measurement:** R6G was selected as the probe molecule. The as-synthesized Au/N-C composite spin-coated on Si substrate was immersed in 5 mL R6G ($10^{-7}$ M) aqueous solutions for 12 h so as to ensure good molecule adsorption, taken out and then dried in air. Raman spectra were recorded on a Renishaw invia Raman Microscopy. The excitation lights were 633 nm from a He-Ne laser beam.

**Photoelectronchemica test:** Photoelectronchemical cells (PECs) measurement was carried out on a CHI 650D electrochemical work station. The working electrode was prepared by drop casting the nanostructures dispersion (4mg/mL) onto F-doped Tin Oxide glass (FTO, 1 cm*1 cm) and then calcined in air at 450 °C for 30 minutes. The counter electrode was a Pt flag and the reference electrode was saturated calomel electrode (SCE). PECs measurement involved the I-V scan technique using a 300 W Xe lamp with a UV light filter ( $\lambda > 420$ nm). For all electrochemical measurements, an aqueous solution of 0.5 M $Na_2SO_4$ was used as the electrolyte.

**Lithium ion battery measurements:** The working electrodes were prepared by mixing the samples ($Fe_2O_3$/N-C), conductive carbon black (Super-P), and poly (vinyldifluoride) (PVDF) at a weight ratio of 80:15:5 and pasted on pure copper foil. Cell assembly was carried out in an Ar-filled glove box with moisture and oxygen concentrations below 1.0 ppm, using lithium metal as the counter electrode. The electrolyte is 1 M $LiPF_6$ in a mixture of ethylene carbonate and diethyl carbonate (1:1 by weight). The cycling and rate performances were recorded on a LAND celltest 2001A system with a voltage of 0.01-3 V vs. $Li^+$/Li.

## Acknowledgements

This work was supported by NSFC (21431003, 91127040, 21221062), and the State Key Project of Fundamental Research for Nanoscience and Nanotechnology (2011CB932402).

## Reference

1. Y. Zhao, R. Nakamura, K. Kamiya, S. Nakanishi, K. Hashimoto, *Nat. Commun*., 2013, **4**, 2390.
2. Q. N. Meng, L. Wang, J. H. Zhang, Y. B. Song, H. Jin, K. Zhang, H. C. Sun, H. Y. Wang, B. Yang, *Angew. Chem. Int. Ed.*, 2013, **52**, 3953-3957.
3. J. Wei, D. D. Zhou, Z. K. Sun, Y. H. Deng, Y. Y. Xia, D. Y. Zhao, *Adv. Funct. Mater*., 2013, **23**, 2322-2328.
4. P. Chen, T. Y. Xiao, Y. H. Qian, S. S. Li, S. H. Yu, *Adv. Mater.*, 2013, **25**, 3192-3196.
5. K. P. Gong, F. Du, Z. H. Xia, M. Durstock, L. M. Dai, *Science*, 2009, **323**, 760-764.
6. Y. G. Li, W. Zhou, H. L. Wang, L. M. Xie, Y. Y. Liang, F. Wei, J. C. Idrobo, S. J. Pennycook, H. J. Dai, *Nat. Nano*., 2013, **7**, 394-400.
7. (a)Y. Li, Y. Zhao, H. H. Cheng, Y. Hu, G. Q. Shi, L. M. Dai, L. T. Qu, *J. Am. Chem. Soc*., 2011, **134**, 15-18; (b) C. L. Han, S. P. Wang, J. Wang, M. M. Li, J. Deng, H. R. Li, Y. Wang, *Nano Res.*, 2013, **12**, 1809-1819.
8. (a) S. B. Yang, X. L. Feng, X. C. Wang, K. Mullen, *Angew. Chem. Int. Ed*., 2011, **50**, 5339-5343; (b) Z. Y. Liu, G. X. Zhang, Z. Y. Lu, X. Y. Jin, Z. Chang, X. M. Sun, *Nano Res.*, 2013, **4**, 293-301.
9. (a) L. G. Bulusheva, A. V. Okotrub, A. G. Kurenya, H. K. Zhang, H. J. Zhang, X. H. Chen, H. H. Song, *Carbon,* 2011, **49**, 4013-4023; (b) K. Zhang, Z. Hu, Z. L. Tao, J. Chen, *Sci. China Mater.*, 2014, **1**, 42-58.
10. C. D. Liang, Z. J. Li, S. Dai, *Angew. Chem. Int. Ed.*, 2008, **47**, 3696-3717.
11. Z. J. Ding, L. Zhao, L. M. Suo, Y. Jiao, S. Meng, Y. S. Hu, Z. X. Wang, L. Q. Chen, *Phys. Chem. Chem. Phys.*, 2011, **13**, 15127-15133.
12. D. Lepage, C. Michot, G. Liang, M. Gauthier, S. B. Schougaard, *Angew. Chem. Int. Ed*., 2013, **50**, 6884-6887.
13. W. Chen, R. B. Rakhi, L. B. Hu, X. Xie, Y. Cui, H. N. Alshareef, *Nano Lett*., 2011, **11**, 5165-5172.
14. C. Wu, X. Y. Huang, X. F. Wu, R. Qian, P. K. Jiang, *Adv. Mater.*, 2013, **25**, 5658-5662.
15. J. Ge, H. B. Yao, X. Wang, Y. D. Ye, J. L. Wang, Z. Y. Wu, J. W. Liu, F. J. Fan, H. L. Gao, C. L. Zhang, S. H. Yu, *Angew. Chem. Int. Ed.*, 2013, **52**, 1654-1659.
16. H. B. Yao, J. Ge, C. F. Wang, X. Wang, H. Hu, Z. J. Zheng, Y. Ni, S. H. Yu, *Adv. Mater.*, 2013, **25**, 6692-6998.
17. Y. Yu, J. F. Zeng, C. J. Chen, Z. Xie, R. S. Guo, Z. L. Liu, X. C. Zhou, Y. Yang, Z. J. Zheng, *Adv. Mater.*, 2014, **26**, 810-815.
18. B. Kong, J. Tang, Z. X. Wu, J. Wei, H. Wu, Y. C. Wang, G. F. Zheng, D. Y. Zhao, *Angew. Chem. Int. Ed*., 2014, **53**, 2888-2892.
19. T. Fukaya, H. Watando, S. Fujieda, S. Saya, C. M. Thai, M. Yamamoto, *Polym. Degrad. Stabil.*, 2006, **91**, 2549-2553.
20. C. H. Zhang, L. Fu, N. Liu, M. H. Liu, Y. Y. Wang, Z. F. Liu, *Adv. Mater.*, 2011, **23**, 1020-1024.
21. W. Ai, Z. M Luo, J. Jiang, J. H. Zhu, Z. Z. Du, Z. X. Fan, L. H. Xie, H. Zhang, W. Huang, T. Yu, *Adv. Mater.*, 2014, **26**, 6186-6192.
22. X. M. Sun, Y. D. Li, *Angew. Chem. Int. Ed.*, 2004, **43**, 597-601.
23. W. Li, Z. H. Zhang, B. Kong, S. S. Feng, J. X. Wang, L. Z. Wang, J. P. Yang, F. Zhang, P. Y. Wu, D. Y. Zhao, *Angew. Chem. Int. Ed.*, 2013, **52**, 8151-8155.
24. H. Lee, S. M. Dellatore, W. M. Miller, P. B. Messersmith, *Science*, 2007, **318**, 426-430.
25. Q. Yue, M. H. Wang, Z. K. Sun, C. Wang, C. Wang, Y. H. Deng, D. Y. Zhao, *J. Mater. Chem. B*, 2013, **1**, 6085-6093.
26. L. Xia, Z. X. Wei, M. X. Wan, *J. Colloid Interface Sci.*, 2010, **341**, 1-11.
27. J. Yan, L. P. Yang, M. F. Lin, J. Ma, X. H. Lu, P. S. Lee, *Small*, 2013, **9**, 596-603.
28. A. Postma, Y. Yan, Y. J. Wang, A. N. Zelikin, E. Tjipto, F. Caruso, *Chem. Mater.*, 2009, **21**, 3042-3044.
29. S. Liu, J. Q. Tian, L. Wang, Y. W. Zhang, X. Y. Qin, Y. L. Luo, A. M. Asiri, A. O. Al-Youbi, X. P. Sun, *Adv. Mater.*, 2012, **24**, 2037-2041.
30. Y. J. Kang, K. J. Erickson, T. A. Taton, *J. Am. Chem. Soc.*, 2005, **127**, 13800-13801.

31. (a) L. Polavarapu, Q. H. Xu, *Langmuir,* 2009, **24**, 10608-10611; (b) M. K. Hossain, G. Willmott, P. Etchegoin, R. Blaikie, J. Tallon, *Nanoscale*, 2013, **5**, 8945-8950.
32. Y. J. Kang, T. A. Taton, *Angew. Chem. Int. Ed.*, 2005, **44**, 409-412.
33. A. C. Templeton, J. J. Pietron, R. W. Murray, P. J. Mulvaney, *J. Phys. Chem. B*, 2000, **104**, 564-570.
34. P. H. Luo, C. Li, G. Q. Shi, *Phys. Chem. Chem. Phys.*, 2012, **14**, 7360-7366.
35. (a) F. Li, Y. F. Huang, Y. Ding, Z. L. Yang, S. B. Li, X. S. Zhou, F. R. Fan, W. Zhang, Z. Y. Zhou, D. Y. Wu, B. Ren, Z. L. Wang, Z. Q. Tian, *Nature*, 2012, **464**, 392-395; (b) A. Chung, Y. S. Huh, D. Erickson, *Nanoscale*, 2011, **3**, 2903-2908.
36. Y. Hu, X. H. Gao, L. Yu, Y. R. Wang, J. Q. Ning, S. J. Xu, X. W. Lou, *Angew. Chem. Int. Ed.,* 2013, **52**, 5636-5639.
37. M. Hu, S. Furukawa, R. Ohtani, H. Sukegawa, Y. Nemoto, J. Reboul, S. Kitagawa, Y. Yamauchi, *Angew. Chem. Int. Ed.,* 2012, **51**, 984-988.
38. S. Grugeon, S. Laruelle, L. Dupont, J. M. Tarascon, *Solid State Sci.,* 2003, **5**, 895-904.
39. J. S. Do, C. H. Weng, *J. Power Sources*, 2005, **146**, 482-486.
40. Y. M. Sun, X. L. Hu, W. Luo, F. F. Xia, Y. H. Huang, *Adv. Func. Mater.*, 2013, **23**, 2436-2444.
41. C. X. Peng, B. D. Chen, Y. Qin, S. H. Yang, C. Z. Li, Y. H. Zuo, S. Y. Liu, J. H. Yang, *ACS Nano*, 2012, **6**, 1074-1081.
42. W. Wei, S. B. Yang, H. X. Zhou, I. Lieberwirth, X. L. Feng, K. Müllen, *Adv. Mater.*, 2013, **25**, 2909-2914.
43. F, Zou, X. L. Hu, Z. Li, L. Qie, C. C. Hu, R. Zeng, Y. Jiang, Y. H. Huang, *Adv. Mater.,* 2014, **26**, 6622-6628.
44. B. Wang, J. S. Chen, H. B. Wu, Z. Y. Wang, X. W. Lou, *J. Am. Chem. Soc.*, 2011, **133**, 17146-17148.
45. (a) L. Zhang, H. B. Wu, S. Madhavi, H. Hng, X. W. Lou, *J. Am. Chem. Soc.*, 2012, **134**, 17388-17391; (b) H. L. Fei, Z. W. Peng, L. L, Y. Y, W. Lu, E. G. Samuel, X. J. Fan, J. Tour, *Nano Res.*, 2014, **4**, 502-510.
46. Z. Y. Wang, D. Y. Luan, S. Madhavi, Y. Hu, X. W. Lou, *Energy Environ. Sci.*, 2012, **5**, 5252-5256.
47. X. H. Cao, B. Zheng, X. H. Rui, W. H. Shi, Q. Y. Yan, H. Zhang, *Angew. Chem. Int. Ed.*, 2014, **53**, 1404-1409.
48. J. M. Jeong, B. G. Choi, S. C. Lee, K. G. Lee, S. J. Chang, Y. K. Han, Y. B. Lee, H. U. Lee, S. Kwon, G. Lee, C. S. Lee, Y. S. Huh, *Adv. Mater.*, 2013, **25**, 6250-6255.
49. B. Xu, Z. C. Zhang, X. Wang, *Nanoscale*, 2013, **5**, 4495-4505.
50. G. Frens, *Nature*, 1973, **241**, 20-22.
51. B. Nikoobakht, M. A. El-Sayed, *Chem. Mater.*, 2003, **15**, 1957-1962.
52. Z. C. Zhang, J. H. Hui, Z. C. Liu, X. hang, J. Zhuang, X. Wang, *Langmuir*, 2012, 28, 14845-14848.
53. X. Wang, Y. D. Li, *J. Am. Chem. Soc.*, 2002. **4**, 2880-2881.
54. L. Q. Chen, X. F. Yang, J. Chen, J. Liu, H. Wu, H. Q. Zhan, C. L. Liang, M. M. Wu, *Inorg. Chem.*, 2010, **49**, 8411-8420.